Extratropical Cyclone Clouds in the GFDL climate model: diagnosing biases and the associated causes

Catherine M Naud[1]

James F Booth[2] and Jeyavinoth Jeyaratnam[2]

Leo J. Donner[3] and Charles J. Seman[3]

Ming Zhao[3], Huan Guo[4], and Yi Ming[3]

[1] Applied Physics and Applied Mathematics, Columbia University/NASA-GISS, New York, NY

[2] Earth and Atmospheric Sciences, City College of the City University of New York, NY

[3] Geophysical Fluid Dynamics Laboratory/NOAA, Princeton, NJ

[4] UCAR/CPAESS, Geophysical Fluid Dynamics Laboratory, Princeton, NJ

contact: cn2140@columbia.edu

Revised for J. Climate

Early Online Release: This preliminary version has been accepted for publication in *Journal of Climate*, may be fully cited, and has been assigned DOI 10.1175/JCLI-D-19-0421.1. The final typeset copyedited article will replace the EOR at the above DOI when it is published.

Abstract

The clouds in southern hemisphere extratropical cyclones generated by the GFDL climate model are analyzed against MODIS, CloudSat and CALIPSO cloud and precipitation observations. Two model versions are used: one is a developmental version of AM4, a model GFDL will utilize for CMIP6, the other is the same model with a different parameterization of moist convection. Both model versions predict a realistic top-of-atmosphere cloud cover in the southern oceans, within 5% of the observations. However, an examination of cloud cover transects in extratropical cyclones reveals a tendency in the models to overestimate high-level clouds (by differing amounts) and underestimate cloud cover at low-levels (again by differing amounts), especially in the post-cold frontal (PCF) region, when compared to observations. Focusing on only the models, their differences in high and mid-level clouds are consistent with their differences in convective activity and relative humidity (RH), but the same is not true for the PCF region. In this region, RH is higher in the model with less cloud fraction. These seemingly contradictory cloud and RH differences can be explained by differences in the cloud parameterization tuning parameters that ensure radiative balance. In the PCF region, the model cloud differences are smaller than either of the model biases with respect to observations, suggesting other physics changes are needed to address the bias. The process-oriented analysis used to assess these model differences will soon be automated and shared.

Accepted for publication in *Journal of Climate*. DOI 10.1175/JCLI-D-19-0421.1.

1. Introduction

Over the past decade, cloud cover biases in the southern hemisphere oceans have been identified (Trenberth and Fasullo 2010) and investigated in a large number of general circulation models (GCMs) and reanalysis products. Bodas-Salcedo et al (2012; 2014) demonstrated that biases in shortwave absorption at the surface (an issue dominating during the austral summer) stem from deficiencies in the low and mid-level clouds typically found in the cold sector of extratropical cyclones. Coincidently Naud et al. (2014) showed that recent versions of reanalyses do not have enough clouds in extratropical cyclone cold sectors. This underestimate in Southern Oceans cloud cover was diagnosed in both Coupled Model Intercomparison Project (CMIP) phase 3 and CMIP5 models, and until recently was found to affect most current models (Bodas-Salcedo et al., 2014). That GCMs do not produce enough cloud in the Southern Oceans is problematic: this causes errors in the amount of shortwave radiation reaching the ocean surface (Trenberth and Fasullo, 2010), biases in atmospheric circulation change predictions (e.g. Ceppi and Hartmann, 2016; Grise and Medeiros, 2016) and ultimately affects climate sensitivity in models (Frey and Kay, 2018). Most specifically for ocean-atmosphere coupled models, the cloud bias can affect Southern Oceans ventilation and the location of the Intertropical Convergence Zone (e.g. Xiang et al., 2018).

One potential reason behind this persistent problem was attributed to the ubiquitous presence of supercooled water in southern hemisphere (SH) clouds (Morrison et al. 2011) which models have problems maintaining (Kay et al., 2016). By forcing their model to maintain liquid in clouds for temperatures below freezing, Kay et al (2016) could correct the surface absorption issue. However, while an advanced treatment of boundary layer clouds in another

Accepted for publication in *Journal of Climate*. DOI 10.1175/JCLI-D-19-0421.1.

model improved southern hemisphere cloud liquid amounts, its cloud cover bias persisted (Wall et al, 2017; Song et al., 2018).

These recent studies focused on both the microphysical and macrophysical aspects of cloud representation but there might be other aspects of model cloud parameterization that need to be investigated before the SH cloud cover bias can be understood and corrected, such as the representation of boundary layer processes and convection. Here we focus on convection. This is motivated in part by recent work of Lamraoui et al. (2019) who find that, at the typical spatial resolution of a GCM, cloud cover in cyclone cold sectors is responding more strongly to changes in the convection than the boundary layer parameterizations. However, these results were obtained with the Weather Research Forecasting model for a single case study, so it is uncertain whether the impact of convection parameterization is as large in a global scale multi-year GCM integration.

Another related issue discussed in the Kay et al (2016) and Frey and Kay (2018) studies resides with the impact of the various parameters that need to be set in the models to keep them in radiative balance. While these parameters are chosen to be as realistic as possible, their exact values are not always precisely known or constant in nature (Hourdin et al., 2017; Schmidt et al., 2017), and small changes in these tuning parameters can have large impacts on cloud cover and other fields important for accurate future temperature predictions (e.g. Golaz et al., 2013; Zhao et al., 2018b), in part because of the nonlinear nature of the model physics.

Because these two issues cannot easily be untangled, the goal of this study is therefore to examine both the impact of the convection parameterization and of the tuning of cloud parameters on the model representation of cloud cover in the cold sector of extratropical

Accepted for publication in *Journal of Climate*. DOI 10.1175/JCLI-D-19-0421.1.

cyclones. To do this, we take advantage of metrics designed to evaluate modelled cloud cover in the cold sector of extratropical cyclones (e.g. Naud et al., 2014, 2015, 2016) and apply them to two separate development versions of the Geophysical Fluid Dynamics Laboratory (GFDL) Atmosphere model version 4 (AM4). These two versions were produced at different stages of the latest GFDL AM4 model development (Zhao et al., 2018a,b), one of the major US climate models slated to be part of the next Model Intercomparison Project phase 6 exercise. The main differences that matter for the clouds between the two model versions are: the parameterization of convection and the tuning applied in the cloud parameterization that ensures radiative balance. The convective parameterizations are: a two-plume model as used in the most recent release of the model AM4.0 described in Zhao et al. (2018a,b) and a multi-plume model as described in Donner et al. (2011).

Herein, we compare both versions of the model to cloud cover observations obtained with the Moderate resolution Imaging Spectroradiometer (MODIS; Salomonson et al., 1989) and the two active instruments onboard CloudSat (Stephens et al, 2002) and CALIPSO (Winker et al. 2009). The methodology is based on compositing, using the center of extratropical cyclones as anchors to obtain the mean cloud cover for a large number of systems, which was shown to be a useful method for comparison with free-running models (e.g. Klein and Jakob, 1999; Bauer and Del Genio, 2006; Field et al., 2008, 2011; Govekar et al., 2014). We also introduce cold front centered vertical transects, which have also been used for model evaluation (Naud et al., 2010; Booth et al., 2013). These composite transects were found particularly useful when using CloudSat-CALIPSO observations which provide full cloud profiles but, with their narrow footprint, only partly sample frontal regions. The focus is on the cold frontal regions of

Accepted for publication in *Journal of Climate*. DOI 10.1175/JCLI-D-19-0421.1.

extratropical cyclones located in the Southern Oceans during the warm season (when insolation is at a maximum).

2. Model, observations and methodology

For model and observations, the analysis is performed only from November to March and solely for the southern hemisphere oceans.

2.1 Model description

The versions of the GFDL model examined here are intermediate development versions of the GFDL model that precedes AM4.0 (Zhao et al., 2018a, 2018b), and generically referred to as devAM4. The focus is the parameterization of convection and both devAM4 and AM4.0 represent convection using the same modified mass flux scheme originally developed for shallow convection (Bretherton et al. 2004). The original Bretherton et al (2004) scheme utilizes a single bulk plume which entrains and detrains at each model layer. While the lateral mixing rate is largely specified, the vertical profile of entrainment/detrainment rate is determined interactively by a parcel buoyancy sorting algorithm so that the cloud vertical mass flux can either increase or decrease with height depending on the thermodynamic properties of cloud environment.

Attempts at using the single bulk plume model for representing both shallow and deep convection met with some success at a high (50km) resolution (Zhao et al., 2009). However, during the development of AM4/CM4, it was found that some aspects of coupled model biases (e.g., equatorial Pacific cold bias) could be significantly reduced by including an additional deep plume with a reduced lateral mixing rate. The motivation of including such an additional deep

Accepted for publication in *Journal of Climate*. DOI 10.1175/JCLI-D-19-0421.1.

plume is discussed in Zhao et. al (2016) and Zhao et. al (2018b). Below we refer to this 2 plume scheme as devAM4-2PM, or simply 2PM.

We obtained output from a predecessor version of the devAM4 model that uses, amongst other differences, a distinct scheme for the parameterization of convection than in devAM4-2PM. This second model version still uses the Bretherton et al (2004) parameterization for shallow convection, but handles deep convection with a scheme introduced by Donner et al. (2001), which is a multi-plume model (Donner et al., 2011). Therefore, this second version of the model will be referred to as the multi-plume model devAM4-MPM, or MPM.

The devAM4 has the same overall physics parameterizations as AM4.0, however there are a number of differences in the configuration of the parameterizations. More specifically, we list here the components that differ from what is described in Zhao et al. (2018b): 1) the treatment of convective precipitation and cumulus mixing in devAM4 is similar to that described in Zhao et. al (2016). The total condensate is removed as precipitation, which is then partitioned into liquid and ice phase based on temperature. In addition, the parameterization of lateral mixing rate of the shallow plume was simplified by removing its height dependence; 2) the devAM4 uses a 4-stream treatment of shortwave (SW) radiation with a SW radiation time-step of 2 hours. This choice was not adopted in AM4.0 because of its significant computational cost with little improvement in simulations of radiation fields; 3) The decorrelation length scale in the cloud overlap assumption is set to 1 km in devAM4; 4) the size distribution of sulfate aerosol for computing cloud drop activation in devAM4 follows that described in Donner et al. (2011); 5) the devAM4 has 32 vertical layers instead of the 33 layers used in AM4.0; 6) convection in stratocumulus clouds can be overactive in the model, so, for AM4.0, convection is turned off

Accepted for publication in *Journal of Climate*. DOI 10.1175/JCLI-D-19-0421.1.

147 whenever the Wood and Bretherton (2006) Estimated Inversion Strength parameter exceeds 8
148 K. This test is not implemented in devAM4.

149 Changing the convection scheme changes the thermodynamics and dynamics in the model,
150 which impacts the clouds and radiation. As such, if we performed integrations using devAM4
151 with only the convection scheme changed, the model would be significantly inconsistent with
152 the present-day Earth energy imbalance of around 0.7 Wm^{-2} (Schmidt et al., 2017). Such a
153 model would not be consistent with all GCMs utilized in IPCC experiments, and the
154 interpretation of the physics would be subject to a strong caveat: a lack of radiative balance.
155 Therefore, some tuning parameters that impact clouds and precipitation had to be changed in
156 MPM, as compared to 2PM, so that MPM is in radiative balance as well. So in the rest of the
157 study, when we mention tuning, we mostly refer to the parameters used in the cloud
158 parameterization (other than moist convection). To help decipher differences between 2PM
159 and MPM that are the consequence of a differing convection scheme rather than cloud tuning
160 parameters, we also introduce two additional model integrations that are out of radiative
161 balance: one devAM4 version with the 2PM convection scheme but tuned with the MPM tuning
162 parameters, hereafter referred to as "2PM (MPM Tune)", and devAM4 with the MPM
163 convection scheme but tuned with 2PM tuning parameters, referred to as "MPM (2PM Tune)".
164 These supplemental integrations can be considered as an attempt at keeping as much of the
165 MPM/2PM model characteristics but for the convection scheme. That is to say MPM (2PM
166 Tune) includes as many of the 2PM model characteristics as possible but uses the MPM
167 convection scheme (and inversely). The four model integrations examined here are summarized
168 in Table 1.

Accepted for publication in *Journal of Climate*. DOI 10.1175/JCLI-D-19-0421.1.

169 The primary cloud parameterization tuning differences between MPM and 2PM that are
170 relevant to our comparison are (see details in Table 2): (1) a larger volume-mean drop radius for
171 autoconversion of cloud liquid to rain in MPM (10 vs. 8 μm); (2) a larger lower bound on the
172 stratiform sub-grid vertical-velocity standard deviation used for aerosol activation to cloud
173 droplets in MPM (0.7 versus 0.3 ms^{-1}); (3) a more rapid erosion of stratiform clouds in 2PM
174 (erosion constants 10 to 140 times larger, depending on whether stratiform clouds co-occur
175 with various combinations of diffusion and convection); (4) the ice crystal fall speeds in MPM
176 are two-thirds of those in 2PM; (5) the boundary-layer cloud-top radiative cooling generates
177 more entrainment into the boundary-layer in MPM than 2PM (buoyancy parameter related to
178 radiation 20% larger); (6) the entrainment in shallow cumulus plumes is 90% larger in MPM
179 than 2PM; and (7) precipitation efficiencies in shallow cumulus plumes are lower in 2PM, e.g.,
180 about 25% of the efficiencies in MPM around 800 hPa. As we discuss the differences in clouds
181 for the two models, we will refer back to the changes in tuning parameters to point out when
182 they might be contributing to the changes we find.
183 Both model versions were run for the same time period (2008-2012) and with the same sea
184 surface temperature forcing. The output used here is available at 1.25°x1° spatial resolution
185 every 6 hours and consist of: 2D total cloud cover, surface precipitation (total, large-scale and
186 convective), column integrated precipitable water, 500 hPa vertical velocity and sea level
187 pressure, as well as vertical profiles on model levels of cloud cover (total, large-scale and
188 convective), geopotential heights, temperature tendencies for convection, relative humidity,
189 temperature, and wind.

Accepted for publication in *Journal of Climate*. DOI 10.1175/JCLI-D-19-0421.1.

Finally, GFDL has implemented the Cloud Feedback Model Intercomparison Project (CFMIP) Observation Simulator Package (COSP; Bodas-Salcedo et al., 2011) in its latest operational AM4.0 model (Zhao et al., 2018a). The COSP simulators are developed to take into account known limitations in the observations when comparing with modelled output. However the simulators were not implemented in the model development versions examined here. Because our focus here is on differences between two different models, the observations are merely used as a benchmark, and are not intended to provide an absolute truth. Therefore, the lack of COSP simulated output is not an impediment for the study and does not qualitatively affect the results and conclusions.

2.2 Observations

To provide a reference for comparison with model output, cloud observations retrieved with MODIS and CloudSat-CALIPSO are used, and meteorological fields (i.e. temperature, wind, precipitable water and vertical velocities) are obtained from the MERRA-2 reanalysis (Gelaro et al., 2017).

In this study, we use both monthly and daily gridded *Aqua* MODIS cloud fraction products (Menzel et al., 2008) from the latest (collection 6) processing algorithm. This cloud fraction product is initially calculated for 5 km pixels using the 1 km cloud mask (Ackerman et al., 2008) obtained using a series of observed radiances in the visible and infrared channels. The instantaneous 5 km resolution cloud fraction retrievals are then aggregated for the monthly and daily files into a grid of 1° x 1° spatial resolution, for all day and night time orbits, and all cloud types. This product's known limitations are misdetections over snow and sea ice, in the sunglint region and at low sun and view angles (Menzel et al., 2008). An evaluation of the

Accepted for publication in *Journal of Climate*. DOI 10.1175/JCLI-D-19-0421.1.

MODIS cloud fraction retrievals in extratropical cyclones regions revealed agreements with other similar products within 5% for the southern oceans, but also issues over sea ice and snow covered land which we do not include here (Naud et al. 2013). However, because of the latitudes considered here and the focus on warm months, we expect a minimal impact of these issues on the results. Here we refer to these cloud fractions as total cloud cover to match the model syntax. We collected monthly and daily data for the period overlapping with the model run, 2008-2012.

The CloudSat-CALIPSO cloud profiles are obtained from the GEOPROF-LIDAR product (Mace and Zhang, 2014), which reports up to 6 cloud layer base and top altitudes in each CloudSat footprint (~1.4 km x 1.7 km; Tanelli et al, 2008). These cloud layer boundaries are obtained by combining CALIPSO and CloudSat cloud mask products. Here they are used to produce a vertical cloud mask of 250 m vertical resolution along the CloudSat orbits. This product is known to experience issues close to the surface because of ground clutter, so the first kilometer above sea-level is not examined here. Also, cloud and precipitation cannot be distinguished, so cloud extents can be overestimated, i.e. cloud base might be too low. Here we collected all the data for the period 2006-2016, but after 2011, the CloudSat radar platform is only operated during daytime. This was found not to affect the analysis (not shown).

Shortwave (SW) and longwave (LW) top-of-atmosphere cloud radiative effect (CRE) are obtained from the NASA Clouds and the Earth's Radiant Energy System (CERES) Energy Balanced and Filled (EBAF) Edition 4.0 product (Loeb et al, 2018).

2.3 Extratropical cyclones and cold front identification.

Accepted for publication in *Journal of Climate*. DOI 10.1175/JCLI-D-19-0421.1.

Two distinct algorithms are used to 1) identify and track extratropical cyclones and 2) locate cold fronts. The cyclones are identified with the Modeling, Analysis and Prediction (MAP) Climatology of Midlatitude Storminess (MCMS) algorithm (Bauer et al., 2016) which uses 6-hourly gridded sea level pressure fields to locate storm centers and then track them through the cyclone lifetime. This algorithm has historically been used to create a database of cyclone locations using the ERA-interim reanalysis (Dee et al., 2011), here we collected locations for the period 2006-2016 to match the two cloud datasets described above. The same MCMS algorithm is also applied to the four models (c.f. table 1) sea level pressure fields.

Both 2PM and MPM exhibit a similar total number of 6-hourly cyclone detections. However, MPM tends to detect more cyclone centers north of 40°S while 2PM detects more south of 50°S. These differences in location cause differences in environmental moisture in the vicinity of the cyclones (which in turn can impact cloud cover). This is despite using the same fixed SST forcing in both models. Consequently, when we compare the two model versions, we impose a similar zonal distribution of cyclones in both models. For this, we randomly select cyclone centers in 2° wide latitude bands to ensure the same total number of cyclones per band in each model.

Cold fronts are identified using an algorithm described in Naud et al. (2016). It is applied to MERRA-2 850 hPa potential temperature gradients using the Hewson (1998) technique to identify cold fronts. For cyclones that have temperature gradients too weak to allow the routine to identify the cold fronts, the method proposed by Simmonds et al (2012) is applied instead, also using MERRA-2 output. This method locates surface cold fronts based on the change in 850 hPa wind direction and strength as a cold front passes a location. The MERRA-2

Accepted for publication in *Journal of Climate*. DOI 10.1175/JCLI-D-19-0421.1.

reanalysis was chosen because of its relatively high spatial resolution (0.625° x 0.5°) that helps obtain more precise frontal locations. The MERRA-2 based cold front identifications are used with cloud observations. The same Naud et al. (2016) algorithm is applied to the four integrations of the devAM4 model (c.f. table 1), making use of the modeled 850 hPa potential temperature and winds.

2.4 Compositing method

We use composites of cloud cover, as well as other atmospheric variables, over multiple instances of the same type of atmospheric phenomenon to compare the models to observations or reanalysis. We generate two types of composite averages: cyclone centered and cold front centered. The former is a plan view as a passive instrument would observe, while the latter is a vertical transect spanning both sides of the cold front as observed by active instruments. Composites are an average, as such all variability is smoothed out and the resulting distributions are representing the most salient features and do not necessarily look like any of the individual cases that went into it. However, they present a great advantage for model evaluation as they allow multiple cases to be included and do not necessitate a match in time and space between the free running models and observations.

The cyclone-centered composites are constructed using the same stereographic grid for model output, MERRA-2 products, and MODIS observations, centered on the low pressure minimum of a cyclone, of 100 km radial and 15° angular resolution, and extending out to 2500 km radially (e.g. Naud et al., 2014). Model output or observations are projected onto this grid for each 6-hourly cyclone detected in the model or with reanalysis, and the composite shows the average of all cyclones calculated by superimposing the centers on top of each other. Here

Accepted for publication in *Journal of Climate*. DOI 10.1175/JCLI-D-19-0421.1.

277 we composite total cloud cover, precipitable water (PW) and 500 hPa vertical velocity. For this
278 study, the cyclone-centered composites have been flipped to place the polar side of the
279 cyclones at the top of the figure. We acknowledge that this is a northern hemisphere centric
280 approach.

281 The cold-front-centered composite grid is assumed to be perpendicular to the surface front,
282 of 100 km horizontal and 1 km vertical resolution for both the observations and the model
283 output (to accommodate for the coarser resolution of the model levels aloft), extends ±1500
284 km along the horizontal (the zero point is anchored on the surface front), and spans a 15 km
285 vertical extent above sea level (Naud et al., 2015). The observations are sparse in the cold
286 frontal region, so we collect any CloudSat footprint that is found within a region 3000 km wide
287 (i.e. within 1500 km of the front) and of the cold front length (c.f. Naud et al., 2015 for more
288 details on the method). The distance between the profiles and the surface front is used to
289 allocate the CloudSat-CALIPSO cloud mask profile to a given composite grid box. Some CloudSat
290 orbits might intersect the cold front, but this is not a necessary condition. For the model
291 output, the vertical cloud cover profiles are also collected in the 3000 km wide box centered on
292 the cold front and allocated to the composite grid in the same fashion as the observations. The
293 difference is that all profiles in the box are used for the model composites, while the
294 observations are only available along the CloudSat orbit. Another condition that is applied to
295 both observations and model output is that the cloud profile must be outside a 500 km radius
296 region centered on the low pressure minimum of the parent cyclone to avoid contamination by
297 the wrap around region and occluded quadrant. The model output that are also composited in

Accepted for publication in *Journal of Climate*. DOI 10.1175/JCLI-D-19-0421.1.

these cold-front centered transects are the relative humidity and the temperature tendencies for convection.

3. Comparison between modeled and observed cloud cover

The cloud cover comparison is performed in three separate point of view: large scale for the entire ocean basin, at the scale of extratropical cyclones and at the scale of cold frontal regions.

3.1 Large scale cloud cover and cloud radiative effect in the southern oceans

As a preliminary test, we evaluate the total annual mean cloud cover in the southern oceans produced by the two versions of the model. For reference, we use a 5-year mean of MODIS monthly observations for 2008-2012. In addition, we use CERES longwave and shortwave cloud radiative effect (CRE) estimates to evaluate the CRE from both model versions. According to MODIS retrievals, cloud cover is greater than 85% over the southern oceans between 44° and 64°S, with a thinner band of cloud cover exceeding 95% south of 50°S (Figure 1a). This is consistent with a longer period of MODIS observations and another instrument (Naud et al, 2014). Both versions of the model also find a relative maximum at these latitudes, but 2PM is biased low by about 5% (Figure 1b) while MPM is biased high, also by about 5% (Figure 1c). While the two versions of the model are fairly close to observations (and actually within observational uncertainties, c.f. Naud et al. 2014), they differ from one another by a much larger amount than their individual departure from observations.

The implication of these differences can be examined with the longwave and shortwave cloud radiative effect (Figure 2). Both model versions tend to predict a larger magnitude of the SW CRE than what is produced with CERES (Fig 2a), with a larger bias for 2PM (Fig 2c vs. 2e).

Accepted for publication in *Journal of Climate*. DOI 10.1175/JCLI-D-19-0421.1.

This suggests that the modelled clouds are optically thicker than observed, and that 2PM clouds are optically thicker than MPM clouds to compensate for the lower cloud cover. In contrast, both models predict a lower magnitude of the LW CRE than observed with CERES (Fig 2b), but MPM is closer to the observations than 2PM (Fig 2f vs. 2d). This suggests that the additional clouds produced with MPM that give larger cloud cover than both 2PM and MODIS are high-level clouds that are optically thin. This is also suggested by the direct comparison of MPM and 2PM SW and LW CRE (Figs 2g, 2h).

Because the area of large cloud cover is strongly impacted by extratropical cyclones (Bodas-Salcedo et al., 2014; Naud et al. 2014), next we focus our attention to the representation of clouds in these systems, and specifically during the warm season (November to March) when the surface shortwave absorption bias is identified (Bodas-Salcedo et al., 2014).

3.2 Cyclone-centered composites of cloud, precipitable water and vertical velocity

Cyclone-centered composites are constructed for total cloud cover, PW and 500-hPa vertical velocities. We remind the reader that the cyclones have been flipped so that the polar side is at the top of the figures. We compare the two model versions to MODIS for total cloud cover and to MERRA-2 for both PW and vertical velocities (Figure 3).

The cyclone-centered composite of MODIS total cloud cover indicates an area of relatively large cloud cover near the storm center, with decreasing cloud cover into the equator side of the center (Figure 3a). Both versions of the model give a similar spatial distribution, but also suggest that the maximum near the center has larger cloud cover in the model than observed (Figure 3b, 3c). The relative minimum in the western-equatorward quadrant reveals lower cloud cover for 2PM than observed (Figure 3b), but larger than observed for MPM (Figure 3c).

Accepted for publication in *Journal of Climate*. DOI 10.1175/JCLI-D-19-0421.1.

342 This suggests that 1) to be consistent with Figures 1 and 2 the larger spatial extent of the region
343 of negative bias in 2PM outweighs the region of positive bias near the center and 2) the biases
344 found in Figure 1 might be related to the biases in the western-equatorward quadrant, which
345 we refer to as the post-cold frontal region (e.g. Naud et al., 2016). The distribution of PW in the
346 cyclones is typically larger on the equator than polar side of the cyclones, and shows a comma-
347 like structure, coinciding with the region of warm air (i.e. the warm sector), with a maximum in
348 the eastern-equatorward quadrant (Figures 3d-f). There are great similarities between MERRA-
349 2 (Figure 3d) and both model versions, with MPM slightly drier in the warm sector (Figure 3f)
350 than MERRA-2 or 2PM. Finally, 500 hPa vertical velocities indicate a comma-shaped region of
351 strong ascent to the east of the low and a region of subsidence to the west (Figure 3g-i), and
352 both model versions agree with MERRA-2 distribution. This said, the ascent appears to be
353 stronger in the two versions of the model than in MERRA-2.
354 To quantify the differences between the models and observations/reanalysis, we examine
355 composite differences (Figure 4). Both model versions produce a larger cloud cover than
356 observed near the center of the cyclone into the warm sector, with differences around 5 % for
357 2PM (Figure 4a) and 10 % for MPM (Figure 4b). This might be related to the stronger ascent in
358 devAM4 compared to MERRA2 (Figures 4e and 4f). However, the two versions show different
359 cloud cover biases in the western-equatorward quadrant, with a low bias for 2PM (up to 7%)
360 and a slightly positive bias for MPM (under 5%). This cannot be explained by differences with
361 MERRA-2 in PW (Figures 4c and 4d) as these are less than 0.5 mm or of a sign opposite to the
362 cloud cover bias, nor by differences in the dynamics, again near zero in this quadrant (Figures

Accepted for publication in *Journal of Climate*. DOI 10.1175/JCLI-D-19-0421.1.

4e and 4f). Overall, the differences in cloud cover indicate a contrast between the western and eastern equatorward quadrants of the cyclones.

To obtain more details on the differences we find in the equatorward half of the cyclone region between the two model versions and observations, we next turn to composites across cold fronts and CloudSat-CALIPSO observations: this will help determine which cloud level might cause the total cloud cover differences, and analyze the biases with respect to the location of the cold front.

3.3 Cold frontal transects of cloud cover

Here we examine how clouds are distributed vertically on both sides of the cold fronts. The observations are provided by CloudSat-CALIPSO (Figure 5a). The observations indicate that on the west side of the surface front (i.e. the post-cold frontal region), low-level clouds dominate (< 3 km), and occur up to 44% of the time (Figure 5a). Mid- and high-level clouds occur less than 20% of the time (consistent with Naud et al., 2015; 2018). On the eastern side of the front (i.e. the warm sector), clouds occur at all altitudes (0 to ~ 12 km) 30-40 % of the time as this is the region of the warm conveyor belt (as defined by Browning 1986).

Both model versions show a similar spatial distribution of cloud as observed across the entire cold frontal region (Figures 5b, 5c). However, both underestimate low-level cloud cover in the post-cold frontal region by 10-20% and slightly overestimate mid- and high-level cloud cover by 4-8%. In the warm sector, both versions predict cloud cover similar to the observations, albeit with a low bias of 10-20% at mid- and low-levels and a tendency to predict more high level clouds (at least + 10%).

Accepted for publication in *Journal of Climate*. DOI 10.1175/JCLI-D-19-0421.1.

384 The differences between the model and the observations above 5 km, i.e. greater modeled
385 cloud cover than observed, can help explain the differences found when comparing to MODIS
386 (Figure 4). A top-down view would indeed indicate greater total cloud cover in the model than
387 observed based on differences at high and mid-level regardless of potential deficiency in low-
388 level clouds. However, there are clear differences between the two model versions: MPM
389 predicts a larger cloud cover at low levels in the post-cold frontal region and tends to predict
390 high-level cloud cover at higher altitudes in the warm sector (Fig 5c), with less mid-level clouds
391 than 2PM (Fig. 5b). These differences, and those highlighted when comparing with MODIS
392 observations, suggest that the representation of convection has implications for the correct
393 representation of cloud in extratropical cyclones, and more specifically in cold-frontal regions.
394 However, it is unclear how much cloud parameter tuning differences participate in these
395 differences. So next we explore in more detail the differences between 2PM and MPM to help
396 better understand how convection parameterizations and tuning impact cloud cover in these
397 regions.
398
399 **4. Discussion**
400 The two model versions exhibit cloud differences that are not uniform across the cold
401 frontal region, with 1) larger cloud cover in MPM above 10 km on both sides of the front, 2)
402 lower cloud cover in MPM than 2PM in the warm sector from the surface to 10 km, and 3)
403 larger cloud cover in MPM in the post-cold frontal region at all altitudes mostly in a region
404 between 100 km and 1000 km to the west of the front (Figure 5). When distinguishing cloud
405 cover produced with the large-scale cloud scheme (Figure 6a) from the cloud cover directly

Accepted for publication in *Journal of Climate*. DOI 10.1175/JCLI-D-19-0421.1.

406 produced by the convection scheme (Figure 6b), it appears that large-scale cloud cover
407 dominates, with cloud cover from convection occurring less than 2% of the time. Differences
408 between the two model versions are thus dominated by differences in the large-scale cloud
409 scheme (Figure 6d). The convection scheme still plays an important role in forming the total
410 cloud, because it acts as a source and sink for cloud condensate for the large-scale scheme. We
411 also note that while convective cloud fractions are small, the relative differences in convective
412 cloud cover are large between the two model versions (Figure 6e vs. Figure 6b). Therefore, we
413 will use this discussion to explain how the cloud differences, both the large-scale and
414 convection cloud, relate to differences in the parameterizations and differences in the tuning
415 parameters (detailed in Section 2, and Table 2).

416 **4.1 Differences above 10 km**

417 Above 10km, MPM has more large-scale and convective cloud than 2PM all across the cold
418 frontal transect (pre- and post-frontal zones) (Figures 6d,e), and the same difference occurs for
419 RH (Figure 6f). The larger RH in MPM is most likely a result of deeper convection in MPM than
420 2PM: temperature tendencies from convection are greater above 10 km in MPM than 2PM
421 (Figure 7) and the maximum height of convective plumes is also higher in MPM than 2PM
422 (Figure 8). This increased convection would lead to higher RH, and therefore more clouds above
423 10 km in MPM than 2PM (Figure 5). However, another factor impacting clouds at this height is
424 the lower ice crystal fall speeds in the large-scale cloud scheme in the MPM model version. All
425 of the clouds at this height are ice clouds, and the lower fall speeds means that MPM has a
426 weaker cloud sink than 2PM.

Accepted for publication in *Journal of Climate*. DOI 10.1175/JCLI-D-19-0421.1.

427 The relative impact of the convection scheme and tuning depends on the model base state.
428 When we change the tuning in 2PM, i.e. 2PM (MPM Tune), and compare large scale cloud cover
429 to MPM, the effect of the change in convection scheme is significant above 10 km (Figure 6g).
430 However if the change in convection scheme is applied to a model with 2PM tuning, i.e. MPM
431 (2PM Tune) vs 2PM, while the difference above 10 km is still visible, its magnitude is much
432 smaller (Figure 6p), presumably because the amount of ice at upper levels is depleted more
433 rapidly with the 2PM crystal fall speed. Conversely, the impact of the ice crystal fall speed
434 change is much greater when applied to MPM than 2PM (Figure 6m vs. 6j), presumably because
435 the change affects a larger amount of ice in MPM than 2PM above 10 km because of deeper
436 convection in MPM.

437 **4.2 Differences below 10 km: post-frontal region**

438 Below 10 km, extending down to the surface, MPM has more large-scale cloud than 2PM in
439 the post-cold frontal region (Figure 6d). The differences in convective cloud do not mimic the
440 differences in large-scale cloud (Figure 6e), and even more surprisingly the RH differences in the
441 post-cold frontal region do not match the cloud differences (Figure 6f). Thus, MPM has more
442 large-scale cloud but lower RH in the post-cold frontal zone, as compared to 2PM. These
443 seemingly contrasting differences are most likely related to differences in the cloud sinks for
444 the two configurations. The higher amount of large-scale cloud in MPM is consistent with a
445 larger volume-mean drop radius for precipitation in the MPM large-scale cloud scheme (see
446 discussion for precipitation in section 4.4). The lower amount of large-scale cloud and higher
447 RH in 2PM is consistent with a more rapid erosion of the large-scale clouds in 2PM. By imposing
448 a larger volume-mean drop radius for precipitation and a slower erosion in 2PM (MPM Tune),

Accepted for publication in *Journal of Climate*. DOI 10.1175/JCLI-D-19-0421.1.

greater large-scale cloud cover than in the original 2PM post-cold frontal region is produced (Figure 6j). This also means that for the same set of tuning parameters the 2PM model produces in fact larger cloud cover below 3 km in the post-cold frontal region than MPM (Figure 6g or 6p). In contrast, the MPM convective cloud cover in this area is mostly lower than for 2PM, and it seems to be dominated by the change in convection scheme (e.g. Figure 6h vs 6k). This said, again the order in which the tuning and convection scheme are changed matters (Figure 6n and 6q vs. 6h and 6k).

4.3 Differences below 10 km: pre-frontal region

In the pre-frontal region below 10km, the situation is less complicated. MPM large-scale cloud cover and RH are both lower than 2PM cloud and RH (Figures 6d,6f). Moreover the lower RH in MPM negates the impact of erosion and volume-mean drop radius tuning parameters that cause greater large-scale cloud cover below 2 km for both MPM and 2PM convection schemes (Figures 6j and 6m).

4.4 The relation between cloud and precipitation differences

Precipitation is a sink of moisture, and while MPM is tuned to have a greater precipitation efficiency parameter than 2PM for shallow convection, the treatments for convective microphysics in deep convection are structured differently in MPM and 2PM. This might help retain slightly more convective condensate in the lowest 5 km above the surface in MPM than in 2PM that can then be passed on to the large-scale cloud scheme. In nature, precipitation rates are low in post-cold frontal regions (Naud et al. 2015) and both model versions tend to represent this fairly well (Figure 9a). MPM tends to predict larger precipitation rates than 2PM in the post-cold frontal region but lower precipitation in the warm sector (Figure 9b), with

Accepted for publication in *Journal of Climate*. DOI 10.1175/JCLI-D-19-0421.1.

greater differences in the large-scale than convective precipitation. In fact, while MPM produces convective precipitation more often than 2PM (Figure 9c), in accordance with a greater shallow convective precipitation efficiency, it also produces lower convective precipitation rates than 2PM (Figure 9d), which helps keep the difference in total convective precipitation close to zero (Figure 9b). Therefore, the sink that convective precipitation could be is somewhat similar between the two model versions, with compensating effect of frequency of occurrence and rates when precipitating. In the post-cold frontal region, while MPM tends to produce more large-scale precipitation overall (Figure 9a), it is because the precipitation rates when precipitating (i.e. intensity) are larger than for 2PM (Figure 9d). In fact, large-scale precipitation occurs more often in 2PM (Figure 9c) which could explain the paradox of larger precipitation and cloud cover in MPM. This may be explained by the impact of a larger volume-mean drop radius threshold for MPM to precipitate, so that when it does precipitate in MPM, the intensity is greater (Figure 9d).

5. Conclusions

Using MODIS, CloudSat and CALIPSO observations of cloud cover in extratropical cyclones and cold frontal regions, a recent development version of the GFDL AM4 model (Zhao et al, 2018a,b) is evaluated for two different versions of the convection scheme. One version, referred to as 2PM, is a 2-plume model that uses the Bretherton et al. (2004) convection scheme for both shallow and deep convection (Zhao et al., 2018b). The other scheme, referred to as MPM, is a multi-plume model that handles shallow convection with the same scheme but handles deep convection with the Donner (2001) scheme. Both models predict realistic monthly

Accepted for publication in *Journal of Climate*. DOI 10.1175/JCLI-D-19-0421.1.

493 cloud cover over the Southern Oceans when compared to MODIS, but 2PM predicts about 10%
494 less cloud cover than MPM, i.e. a difference between the two model versions greater than their
495 respective deviation from observations. While MPM shortwave and longwave cloud radiative
496 effects are quite close to observations, 2PM tends to exhibit larger magnitude in shortwave
497 cloud radiative effect but lower magnitude in the longwave. This suggests that while MPM
498 might produce greater cloud coverage, 2PM tends to produce optically thicker clouds, and
499 overall lower cloud top heights. A similar discrepancy in cloud cover between the two models
500 and with observations is found in the cold sector of extratropical cyclones, and more specifically
501 in cold frontal regions.

502 A closer examination of cloud vertical profiles in these cold frontal regions reveals that both
503 model versions overestimate cloud cover at high levels (i.e. above 10 km) but underestimate
504 cloud cover at mid and low level. In the warm sector of the cyclone, this altitude dependent
505 bias is larger for MPM, and is easily explained when examining differences in relative humidity
506 profiles. Both model versions are top heavy for both convective and large-scale cloud fraction,
507 and it is more so in the warm sector and when using the MPM scheme.

508 In the post-cold frontal regions, both model versions underestimate low-level cloud cover
509 but the bias is larger for 2PM. This area of negative bias is in fact the area where convective
510 activity is largest in the entire cold frontal region for both model versions. The convective
511 activity at low levels in the post-cold frontal region is larger but shallower in 2PM than MPM.
512 Because convective cloud cover is much smaller than cloud cover predicted with the large-scale
513 cloud scheme, the convection parameterizations are either too efficient at precipitating or not
514 efficient enough at detraining condensate. These efficiencies are controlled by parameters that

Accepted for publication in *Journal of Climate*. DOI 10.1175/JCLI-D-19-0421.1.

515 can be tuned in the model. Convective detrainment above the boundary layer, lateral mixing
516 effects, stratiform cloud erosion, and precipitation efficiency are different between the two
517 model versions, and these differences are contributing to the discrepancies we have found. In
518 fact, the choices made for the MPM tuning tend to help maintain cloud in the post-cold frontal
519 region. Overall, it seems that both model versions might just be too convectively active, thus
520 preventing the large-scale cloud scheme to be called often enough. This problem was found in
521 stratocumulus cloud regions in a more recent version of the model and corrections have been
522 put in place (Zhao et al, 2018b). Zhao et al (2018b) report issues in the full AM4.0 regarding
523 unrealistically large shallow convective activity in regions of stratocumulus clouds that can
524 cause an underestimate in low-level cloud cover. This problem would also be present in these
525 devAM4 versions. In the released AM4.0 version of this model, this overactivity is counteracted
526 by forcing the model to switch off the convection scheme in favor of the large scale cloud
527 scheme when the Wood and Bretherton (2006) estimated inversion strength (EIS) parameter
528 exceeds 8 K. In Naud et al (2016), post-cold frontal regions were found to exhibit values of EIS
529 much lower than 8 K so it is not clear at this point whether this correction will help predict
530 values of cloud cover in post-cold frontal region closer to the 40-45% indicated by CloudSat-
531 CALIPSO observations.

532 It remains that the relatively more active convection in the post-cold frontal boundary layer
533 is somewhat inhibiting the formation and persistence of clouds in devAM4. However, it appears
534 that tuning plays a significant role. This suggests that while cumulus parameterization is playing
535 a role in the current models difficulties to reproduce a realistic cloud cover in the cold sector of
536 extratropical cyclones, it cannot be excluded as well that both model versions are correct to be

Accepted for publication in *Journal of Climate*. DOI 10.1175/JCLI-D-19-0421.1.

so convectively active in this region. If this is the case then our analysis implies that both convection schemes do not produce enough clouds, and that this might be because of tuning choices.

Despite the numerous differences between extratropical cyclone clouds in the two models, the differences between the low-level, post-cold frontal clouds in either model and CloudSat are substantially larger. Presumably, this bias is related to the fact that both models have too much upper-level cloud in the post-cold frontal region, however, cause and effect for these two issues are hard to discern. The fact that the differences between the two models did not significantly impact these biases points to a need to consider other model physics, such as parameterized vertical transport in the boundary layer. Furthermore, the physics differences between the two configurations compared for this paper are of a similar magnitude as the differences between devAM4 and AM4. Therefore, we cannot expect AM4 to have completely removed the bias in low-level clouds shown here. However, the changes made for AM4, such as removing total condensate as precipitation separately for liquid and ice phase clouds and adding a threshold related to EIS, may contribute to a reduction in the bias.

One goal of this study was to evaluate how sensitive post-cold frontal cloud cover might be to the way convection is parameterized. Doing so in a GCM requires a fine balance between applying substantial changes and maintaining a realistic climate. Therefore the choice of tuning parameters (used for the cloud parameterization) also has a significant impact on the results. While changes in convection scheme and these tuning parameters appear to be additive and lead together to similar output, the same tuning applied to differing model base states can have different effects. Although this is found for a specific model, this should apply to most current

Accepted for publication in *Journal of Climate*. DOI 10.1175/JCLI-D-19-0421.1.

559 climate models of similar resolution. This is because a number of parameters need to be set in
560 cloud parameterizations, and not all are observable, or observations are either scarce or highly
561 uncertain (e.g. Hourdin et al., 2017; Schmidt et 2017).
562 Nevertheless, the work presents a framework that might guide further model development,
563 on convection parameterization as well as other aspects of the model. Moreover, once these
564 cold front oriented metrics developed here can be automated, which is anticipated to be
565 completed in late 2019, modeling centers can use these diagnostics in-line with development.
566
567 **Acknowledgements**
568 This research is funded by NOAA MAP grant number NA15OAR4310094. CMN received
569 additional support from the NASA MAP grant 80NSSC17K0195. The MCMS algorithm and
570 documentation can be found here: gcss-dime.giss.nasa.gov/mcms. The database of cold fronts
571 is available here: portal.nccs.nasa.gov/datashare/Obs-ETC/Fronts-ETC/. The MODIS files were
572 obtained through the LAADS DAAC ladsweb.modaps.eosdis.nasa.gov, the CloudSat-CALIPSO
573 GEOPROF-LIDAR files through the CloudSat data processing center
574 www.cloudsat.cira.colostate.edu, the MERRA-2 products from NASA Goddard Earth Sciences
575 Data and Information Services Center and the ERA-interim products from the European Center
576 for Medium range Weather Forecast website.
577
578
579 **References**

Accepted for publication in *Journal of Climate*. DOI 10.1175/JCLI-D-19-0421.1.

580 Ackerman, S. A., R. E. Holz, R. Frey, E. W. Eloranta, B. C. Maddux and M. McGill, 2008: Cloud
581 detection with MODIS. Part II: Validation. J. Atmos. Ocean. Technol., **25**, 1073-1086.
582 Bauer, M. and A. D. Del Genio, 2006: Composite analysis of winter cyclones in a GCM: influence
583 on climatological humidity. J. Climate, **19**, 1652-1672.
584 Bauer, M.P., G. Tselioudis, and W.B. Rossow, 2016: A new climatology for investigating storm
585 influences in and on the extratropics. J. Appl. Meteorol. Climatol., **55**, 1287-1303.
586 Bodas-Salcedo, A., M. J. Webb, S. Bony, H. Chepfer, J.-L. Dufresne, S. A. Klein, Y. Zhang, R.
587 Marchand, J. M. Haynes, R. Pincus, and V. O. John, 2011: COSP, Satellite simulation
588 software for model assessment. Bull. Amer. Meteorol. Soc., 92, 1023-1043,
589 doi:10.1175/2011BAMS2856.1.
590 Bodas-Salcedo, A., K.D. Williams, P.R. Field, and A.P. Lock, 2012: The Surface Downwelling Solar
591 Radiation Surplus over the Southern Ocean in the Met Office Model: The Role of
592 Midlatitude Cyclone Clouds. J. Climat*e,* 25, 7467–7486, doi.org/10.1175/JCLI-D-11-
593 00702.1
594 Bodas-Salcedo A., K. D. Williams, M. A. Ringer, I. Beau, J. N. S. Cole, J.-L. Dufresne, T. Koshiro, B.
595 Stevens, Z. Wang, and T. Yokohata, 2014: Origins of the solar radiation biases over the
596 Southern Ocean in CFMIP2 Models. *J. Climate*, **27**, 41-56, doi:10.1175/JCLI-D-13-
597 00169.1.
598 Booth J.F., C.M. Naud, and A.D. Del Genio, 2013: Diagnosing warm frontal cloud formation in a
599 GCM: A novel approach using conditional subsetting. *J. Climate*, **26**, 5827-5845,
600 doi:10.1175/JCLI-D-12-00637.1.

Accepted for publication in *Journal of Climate*. DOI 10.1175/JCLI-D-19-0421.1.

601 Bretherton, C. S., McCaa, J. R., & Grenier, H., 2004: A new parameterization for shallow cumulus
602 convection and its application to marine subtropical cloud-topped boundary layers. Part
603 I: Description and 1-D results. Month. Weath. Rev., 132, 864–882.
604 Browning, K. A., 1986: Conceptual models of precipitation systems. Weath. Forec., 1, 23-41.
605 Ceppi P. and D. L. Hartmann, 2016: Clouds and the atmospheric circulation response to
606 warming, J. Climate, 29, 783-799,doi:10.1175/JCLI-D-15-0394.1.
607 Dee, D. P., and co-authors., 2011: The ERA-Interim reanalysis: configuration and performance
608 of the data assimilation systems. Quart. J. R. Meteorol. Soc., **137**, 553-597.
609 Donner, L., Seman, C., Hemler, R., & Fan, S.-M., 2001: A cumulus parameterization including
610 mass fluxes, convective vertical velocities, and mesoscale effects. *J. Climate*, 14, 3444–
611 3463.
612 Donner, L. J., Wyman, B. L., Hemler, R., Horowitz, L. W., & Ming, Y., & Zhao, M., et al., 2011: The
613 dynamical core, physical parameterizations, and basic simulation characteristics of the
614 atmospheric component AM3 of the GFDL global coupled model CM3. *J. Climate*, 24,
615 3484–3519.
616 Field P. R., A. Bodas-Salcedo, and M. E. Brooks, 2011: Using model analysis and satellite data to
617 assess cloud and precipitation in midlatitude cyclones. Quart. J. Roy. Meteorol. Soc.,
618 137, 1501-1515, doi:10.1002/qj.858.
619 Field, P. R., A. Gettelman, R. Neale, R. Wood, P. J. Rasch, and H. Morrison, 2008: Midlatitude
620 cyclone compositing to constrain climate model behavior using satellite observations. *J.*
621 *Climate*, **21**, 5887-5903.

Accepted for publication in *Journal of Climate*. DOI 10.1175/JCLI-D-19-0421.1.

622 Frey W. R. and J. E. Kay, 2018: The influence of extratropical cloud phase and amount feedbacks
623 on climate sensitivity. Clim. Dyn., 50, 3097-3116.
624 Gelaro, R., and co-authors, 2017: The Modern-Era Retrospective Analysis for research and
625 Applications, version 2 (MERRA-2). J. Climate, 30, 5419-5454, doi:10.1175/JCLI-D-16-
626 0758.1.
627 Golaz J.-C., L. W. Horowitz, and H. Levy II, 2013: Cloud tuning in a coupled climate model:
628 Impact on 20th century warming. Geophys. Res. Lett., 40, 2246-2251,
629 doi:10.1002/grl.50232.
630 Govekar, P. D., C. Jakob, and J. Catto, 2014: The relationship between clouds and dynamics in
631 Southern hemisphere extratropical cyclones in the real world and a climate model. *J.*
632 *Geophys. Res.* , **119**, 6609-6628, doi:10.1002/2013JD020699.
633 Grise K. M. and B. Medeiros, 2016: Understanding the varied influence of midlatitude jet
634 position on clouds and cloud radiative effects in observations and global climate models.
635 J. Climate, 29, 9005-9025, doi:10.1175/JCLI-D-16-0295.1.
636 Hewson, T. D., 1998: Objective fronts. *Meteor. Appl.*, **5**, 37–65.
637 Hourdin F., T. Mauritsen, A. Gettelman, J.-C. Golaz, V. Balaji, Q. Duan, D. Folini, D. Ji, D. Klocke,
638 Y. Qian, F. Rauser, C. Rio, L. Tomassini, M. Watanabe, and D. Williamson, 2017: The art
639 and science of climate model tuning, Bull. Amer. Meteorol. Soc., 98, 589-602,
640 doi:10.1175/BAMS-D-15-00135.2.
641 Kay J. E., C. Wall, V. Yettella, B. Medeiros, C. Hannay, P. Caldwell, and C. Bitz, 2016: Global
642 Climate Impacts of fixing the southern ocean shortwave radiation bias in the community
643 earth system model (CESM). J. Climate, 29, 4617-4636, doi:10.1175/JCLI-D-15-0358.1.

Accepted for publication in *Journal of Climate*. DOI 10.1175/JCLI-D-19-0421.1.

644 Klein, S. A. and C. Jakob, 1999: Validation and sensitivities of frontal clouds simulated by the
645 ECMWF model. *Month. Weath. Rev*., 127, 2514-2531.
646 Lamraoui F., J. F. Booth, C. M. Naud, M. Jensen, and K. L. Johnson, 2019: The interaction
647 between boundary layer and convection schemes in a WRF simulation of post=cold
648 frontal clouds over the ARM East North Atlantic Site. J. Geophys. Res.-Atm., 124, 4699-
649 4721, doi:10.1029/2018JD029370.
650 Loeb, N.G., D.R. Doelling, H. Wang, W. Su, C. Nguyen, J.G. Corbett, L. Liang, C. Mitrescu, F.G.
651 Rose, and S. Kato, 2018: Clouds and the Earth's Radiant Energy System (CERES) Energy
652 Balanced and Filled (EBAF) Top-of-Atmosphere (TOA) Edition-4.0 Data Product. *Journal*
653 *of Climate*, Volume **31**, Issue 2 (January 2018) pp. 895-918. doi: 10.1175/JCLI-D-17-
654 0208.1
655 Mace, G. G., and Q. Zhang, 2014: The CloudSat radar-lidar geometrical profile product (RL-
656 GeoProf): Updates, improvements, and selected results. J. Geophys. Res. Atmos., **119**,
657 doi:10.1002/2013JD021374.
658 Menzel, W. P., R. A. Frey, H. Zhang, d. P. Wylie, C. C. Moeller, R. E. Holz, B. Maddux, B. A. Baum,
659 K. I. Strabala, and L. E. Gumley, 2008: MODIS global cloud-top pressure and amount
660 estimation: algorithm description and results. J. Appl. Meteorol. Climatol., **47**, 1175-
661 1198.
662 Morrison A. E., S. T. Siems, and M. J. Manton, 2011: A three-year climatology of cloud-top
663 phase over the southern ocean and north Pacific. J. Climate, 24, 2405-2418,
664 doi:10.1175/2010JCLI3842.1.

Accepted for publication in *Journal of Climate*. DOI 10.1175/JCLI-D-19-0421.1.

665 Naud, C. M., J. F. Booth, and A. D. Del Genio, 2014: Evaluation of ERA-interim and MERRA
666 cloudiness in the Southern ocean. J. Climate, 27, 2109-2124, doi:10.1175/JCLI-D-13-
667 00432.1.
668 Naud, C. M., J. F. Booth, and A. D. Del Genio, 2016: The relationship between boundary later
669 stability and cloud cover in the post-cold-frontal region. J. Climate, 29, 8129-8149,
670 doi:10.1175/JCLI-D-15-0700.1.
671 Naud, C. M., J. F. Booth, D. J. Posselt, and S. C. van den Heever, 2013: Multiple satellite
672 observations of cloud cover in extratropical cyclones. J. Geophys. Res., 118, 9982-9996,
673 doi:10.1002/jgrd.50718.
674 Naud, C.M., A. D. Del Genio, M. Bauer, and W. Kovari, 2010: Cloud vertical distribution across
675 warm and cold fronts in CloudSat-CALIPSO data and a general circulation model. *J.*
676 *Climate*, **23**, 3397-341
677 Naud, C. M., D. J. Posselt, and S. C. van den Heever, 2015: A CloudSat-CALIPSO view of cloud
678 and precipitation properties across cold fronts over the global oceans. J. Climate, **28**,
679 6743-6762.
680 Naud, C. M., D. J. Posselt, and S. C. van den Heever, 2018: Reply to “Comments on ‘ A CloudSat-
681 CALIPSO view of cloud and precipitation properties across cold fronts over the global
682 oceans’”. *J. Climate*, **31**, 2969-2975.
683 Salomonson, V. V., W. L. Barnes, P. W. Maymon, H. E. Montgomery and H. Ostrow , 1989:
684 MODIS: advanced facility instrument for studies of the earth as a system, IEEE Trans.
685 Geosci. Remote Sens., **27**, 145-153.

Accepted for publication in *Journal of Climate*. DOI 10.1175/JCLI-D-19-0421.1.

686 Schmidt, G.A., D. Bader, L.J. Donner, G.S. Elsaesser, J.-C. Golaz, C. Hannay, A. Molod, R. Neale,
687 and S. Saha, 2017: Practice and philosophy of climate model tuning across six U.S.
688 modeling centers. *Geosci. Model Dev.*, **10**, 3207-3223, doi:10.5194/gmd-10-3207-2017.
689 Simmonds I., K. Keay and J. A. T. Bye, 2012: Identification and Climatology of southern
690 hemisphere mobile fronts in a modern reanalysis. *J. Climate*, **25**, 1945-1962.
691 Song, H., Z. Zhang, P.L. Ma, S. J. Ghan, and M. Wang, 2018: An evaluation of marine boundary
692 layer cloud property simulations in the Community Atmosphere Model using Satellite
693 observations: conventional subgrid parameterization versus CLUBB. J. Climate, 31, 2299-
694 2320, doi: 10.1175/JCLI-D-17-0277.1.
695 Stephens, G. L., D. G. Vane, R. J. Boain, G. G. Mace, K. Sassen, Z. Wang, A. J. Illingworth, E. J.
696 O'Connor, W. B. Rossow, S. L. Durden, S. D. Miller, R. T. Austin, A. Benedetti, C.
697 Mitrescu, and the CloudSat Science Team, 2002: The CloudSat mission and the A-TRAIN:
698 A new dimension to space-based observations of clouds and precipitation. Bull. Am.
699 Meteorol. Soc., **83**, 1771-1790.
700 Tanelli, S., S. L. Durden, E. Im, K. S. Pak, D. G. Reinke, P. Partain, J. M. Haynes, and R. T.
701 Marchand, 2008: CloudSat's cloud profiling radar after two years in orbit: Performance,
702 calibration, and processing. IEEE Trans. Geosci. Remote Sens., 46, 3560–3573,
703 https://doi.org/10.1109/TGRS.2008.2002030
704 Trenberth K. E. and J. T. Fasullo, 2010: Simulation of present-day and twenty-first-century
705 energy budgets in the Southern ocean. *J. Climate*, **23**, 440-454,
706 doi:10.1175/2009JCLI3152.1.

Accepted for publication in *Journal of Climate*. DOI 10.1175/JCLI-D-19-0421.1.

Wall C. J., D. L. Hartmann, and P.-L. Ma, 2017: Instantaneous linkages between clouds and large-scale meteorology over the southern ocean in observations and a climate model. J. Climate. 30, 9455-9474, doi: 10.1175/JCLI-D-17-0156.1.

Winker, D.M., M.A. Vaughan, A.H. Omar, Y. Hu, K.A. Powell, Z. Liu, W.H. Hunt, and S.A. Young, 2009: Overview of the CALIPSO Mission and CALIOP Data Processing Algorithms, J. Atmos. Oceanic Technol., **26**, 2310-2323.

Wood R. and C. S. Bretherton, 2006: On the relationship between stratiform low cloud cover and lower-tropospheric stability. J. Climate, 19, 6425-6432.

Xiang B. Q., M. Zhao, Y. Ming, W. D. Yu and S. M. Kang, 2018: Contrasting impacts of radiative forcing in the Southern Ocean versus Southern Tropics on ITCZ position and energy transport in once GFDL climate model. J. Climate, 31, 5609-5628, doi:10.1175/JCLI-D-17-0566.1.

Zhao, M., J. Golaz, I.M. Held, V. Ramaswamy, S. Lin, Y. Ming, P. Ginoux, B. Wyman, L.J. Donner, D. Paynter, and H. Guo, 2016: Uncertainty in Model Climate Sensitivity Traced to Representations of Cumulus Precipitation Microphysics. *J. Climate,* **29**, 543–560, doi:10.1175/JCLI-D-15-0191.1.

Zhao, M., J.-C. Golaz, I. M. Held, H. Guo, V. Balaji, R. Benson et al., 2018a: The GFDL global atmosphere and land model AM4.0/LM4.0: 1. Simulations characteristics with prescribed SSTs. *J. Adv. Model. Earth Syst.*, 10, 691-734, doi:10.1002/2017MS001208.

Zhao, M., J.-C. Golaz, I. M. Held, H. Guo, V. Balaji, R. Benson et al., 2018b: The GFDL global atmosphere and land model AM4.0/LM4.0: 2. Model description, sensitivity studies and tuning strategies. *J. Adv. Model. Earth Syst.*, 10, 735-769, doi:10.1002/2017MS001209.

Accepted for publication in *Journal of Climate*. DOI 10.1175/JCLI-D-19-0421.1.

729 Zhao, M., Held, I. M., Lin, S.-J., & Vecchi, G. A., 2009: Simulations of global hurricane
730 climatology, interannual variability, and response to global warming using a 50 km
731 resolution GCM. Journal of Climate, 22, 6653–6678.
732

Accepted for publication in *Journal of Climate*. DOI 10.1175/JCLI-D-19-0421.1.

733 Tables

734 *Table 1: Summary of the four model integrations: naming convention, cumulus scheme, tuning protocol.*

Model denomination	Cumulus Scheme	Tuning
2PM	Two-Plume model (Zhao et al., 2016; 2018b)	Tuned in general accordance with Zhao et al. (2018b)
MPM	Multi-Plume model (Donner et al., 2001, 2011)	Tuned in general accordance with GFDL practices described in Schmidt et al. (2017)
2PM (MPM tune)	Two-Plume model (Zhao et al., 2016; 2018b)	Tuned in general accordance with GFDL practices described in Schmidt et al. (2017)
MPM (2PM tune)	Multi-Plume model (Donner et al., 2001, 2011)	Tuned in general accordance with Zhao et al. (2018b)

735

736

Accepted for publication in *Journal of Climate*. DOI 10.1175/JCLI-D-19-0421.1.

Table 2: List of the main tuning parameters that differ between the two devAM4 models with values. More details on the role of each parameter are available in Zhao et al. (2018b).

Tuning Parameter	Expected impact	2PM	MPM
Stratiform Cloud Erosion Constants (s^{-1}) Rates of erosion: - when vertical diffusion is active, - when convection is active without vertical diffusion, - when neither convection nor vertical diffusion is active.	Clouds erode more rapidly when larger.	 $4x10^{-5}$, $4x10^{-5}$, $3x10^{-6}$	 $3x10^{-7}$, $3x10^{-6}$, $1x10^{-7}$
Volume mean-drop radius for autoconversion of cloud liquid to rain (µm)	Clouds precipitate more efficiently when smaller.	8	10
Lower bound of the stratiform subgrid vertical velocity standard deviation used for aerosol activation to cloud droplets (ms^{-1})	Cloud drop number concentration tends to increase when larger.	0.3	0.7
Ice crystal fall speed ratio	Ice falls out faster when larger.	1.2	0.8
Constant in function relating boundary-layer cloud top radiative cooling to boundary-layer entrainment	Larger values increase boundary layer entrainment.	0.25	0.3
Entrainment in shallow cumulus plumes (km^{-1})	Reduces convective buoyancy when larger.	3	5.7
Precipitation efficiency parameters (Pa^{-1}): Liquid ice	Clouds precipitate more efficiently when larger.	 $5x10^{-5}$ $11x10^{-5}$	 $20x10^{-5}$ $44x10^{-5}$

Accepted for publication in *Journal of Climate*. DOI 10.1175/JCLI-D-19-0421.1.

List of Figures

Accepted for publication in *Journal of Climate*. DOI 10.1175/JCLI-D-19-0421.1.

763 and 2PM (j, k, l); MPM and MPM (2PM Tune) (m, n, o); MPM (2PM Tune) and 2PM in (p, q,
764 r). The vertical dashed line indicates the location of the surface front: the post-cold frontal
765 or cold side of the front is to the left of this line, while the pre-cold frontal or warm side of
766 the front is to the right. These are southern hemisphere cold fronts during November-
767 March.
768 Figure 7: Cold front centered composites of temperature tendencies for convection from (a)
769 2PM, (b) MPM and (c) the difference between MPM and 2PM. The vertical dashed line
770 indicates the location of the surface front: the post-cold frontal or cold side of the front is
771 to the left of this line, while the pre-cold frontal or warm side of the front is to the right.
772 These are southern hemisphere cold fronts during November-March.
773 Figure 8: Cold front transect vertical distribution of the maximum height of the convective
774 column in (a) 2PM, (b) MPM and (c) difference in height between MPM and 2PM. The
775 vertical dashed line indicates the location of the surface front: the post-cold frontal or cold
776 side of the front is to the left of this line, while the pre-cold frontal or warm side of the
777 front is to the right. These are southern hemisphere cold fronts during November-March.
778 Figure 9: Cold front centered composite of (a) mean precipitation for 2PM (solid) and MPM
779 (dashed) for total (black), convective (red) and large-scale (blue) precipitation and
780 difference between MPM and 2PM in (b) mean precipitation, (c) frequency of
781 precipitation and (d) precipitation rate when precipitating . The vertical dashed line
782 indicates the location of the surface front: the post-cold frontal or cold side of the front is
783 to the left of this line, while the pre-cold frontal or warm side of the front is to the right.
784 These are southern hemisphere cold fronts during November-March.

Accepted for publication in *Journal of Climate*. DOI 10.1175/JCLI-D-19-0421.1.

785

786

Accepted for publication in *Journal of Climate*. DOI 10.1175/JCLI-D-19-0421.1.

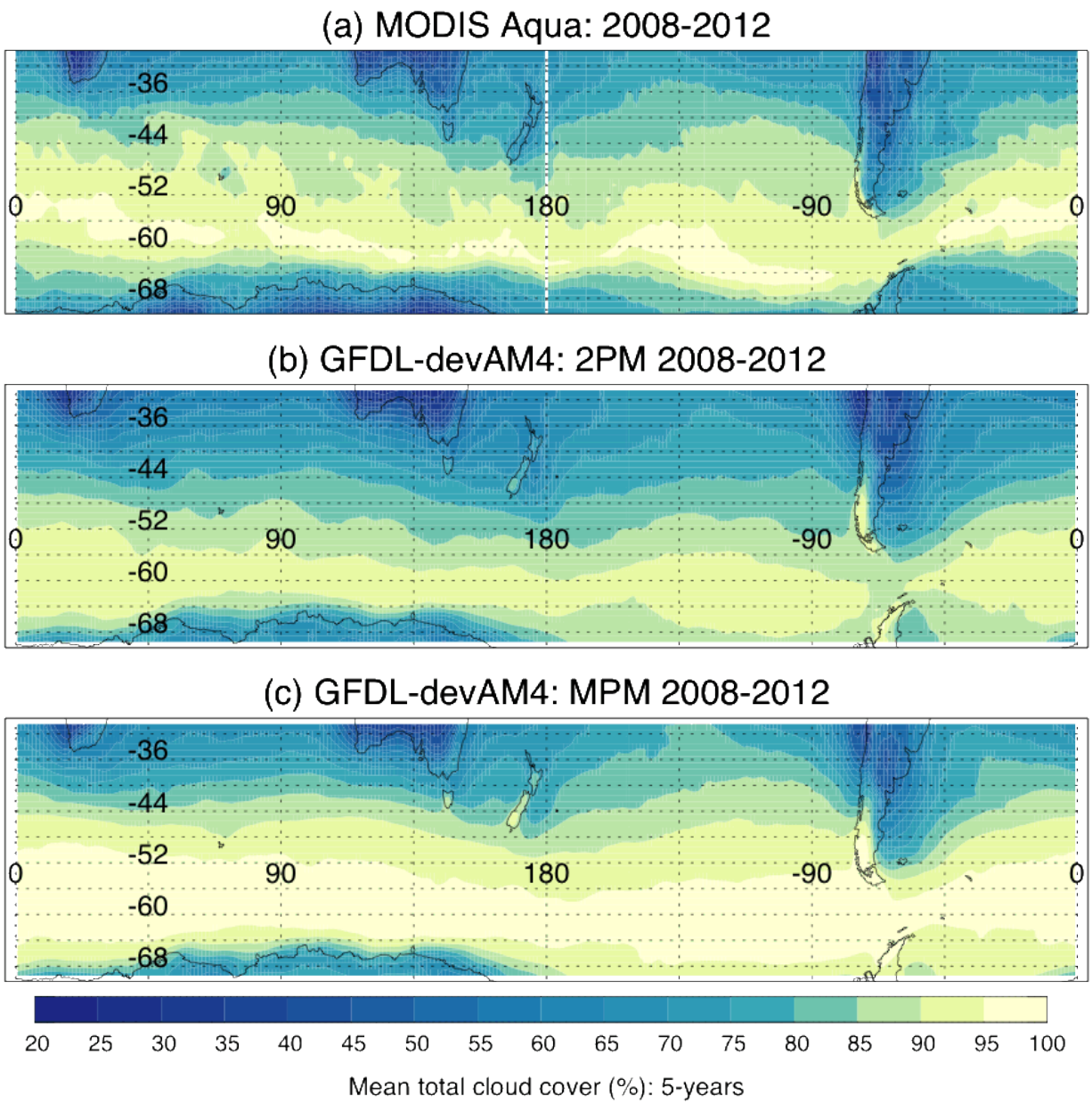

787

788 *Figure 1: 5-year mean total cloud cover for (a) MODIS, (b) devAM4-2PM and (c) devAM4-MPM*
789 *over the southern hemisphere midlatitudes 2008-2012, all months.*

790

Accepted for publication in *Journal of Climate*. DOI 10.1175/JCLI-D-19-0421.1.

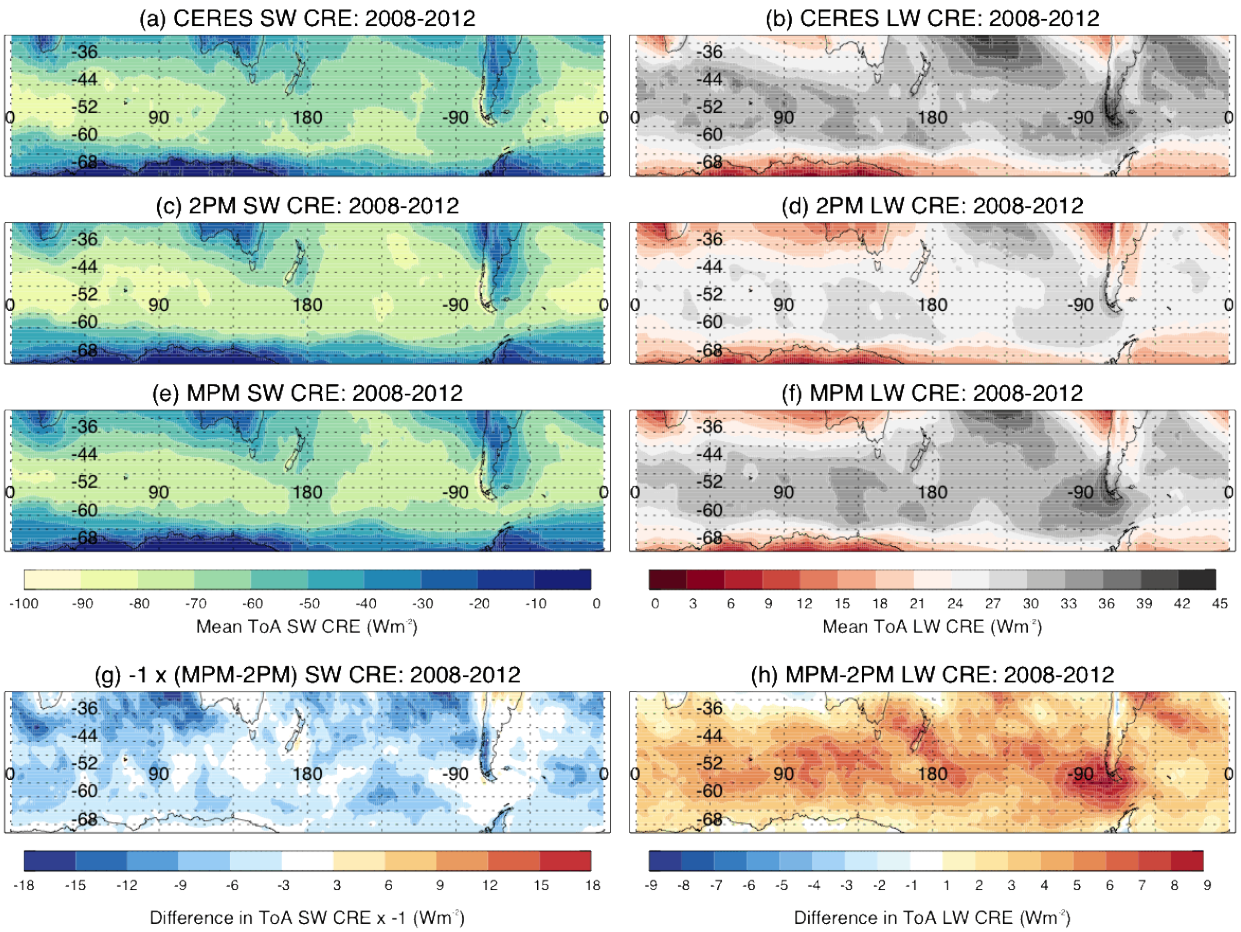

Figure 2: 5-year mean cloud radiative effect (CRE) for (a) CERES shortwave (SW) and (b) CERES longwave (LW), (c) devAM4-2PM SW and (d) devAM4-2PM LW, and (e) devAM4-MPM SW and (f) devAM4-MP LW over the southern hemisphere midlatitudes 2008-2012, all months. Difference between devAM4-MPM and devAM4-2PM (g) SW CRE and (h) LW CRE.

Accepted for publication in *Journal of Climate*. DOI 10.1175/JCLI-D-19-0421.1.

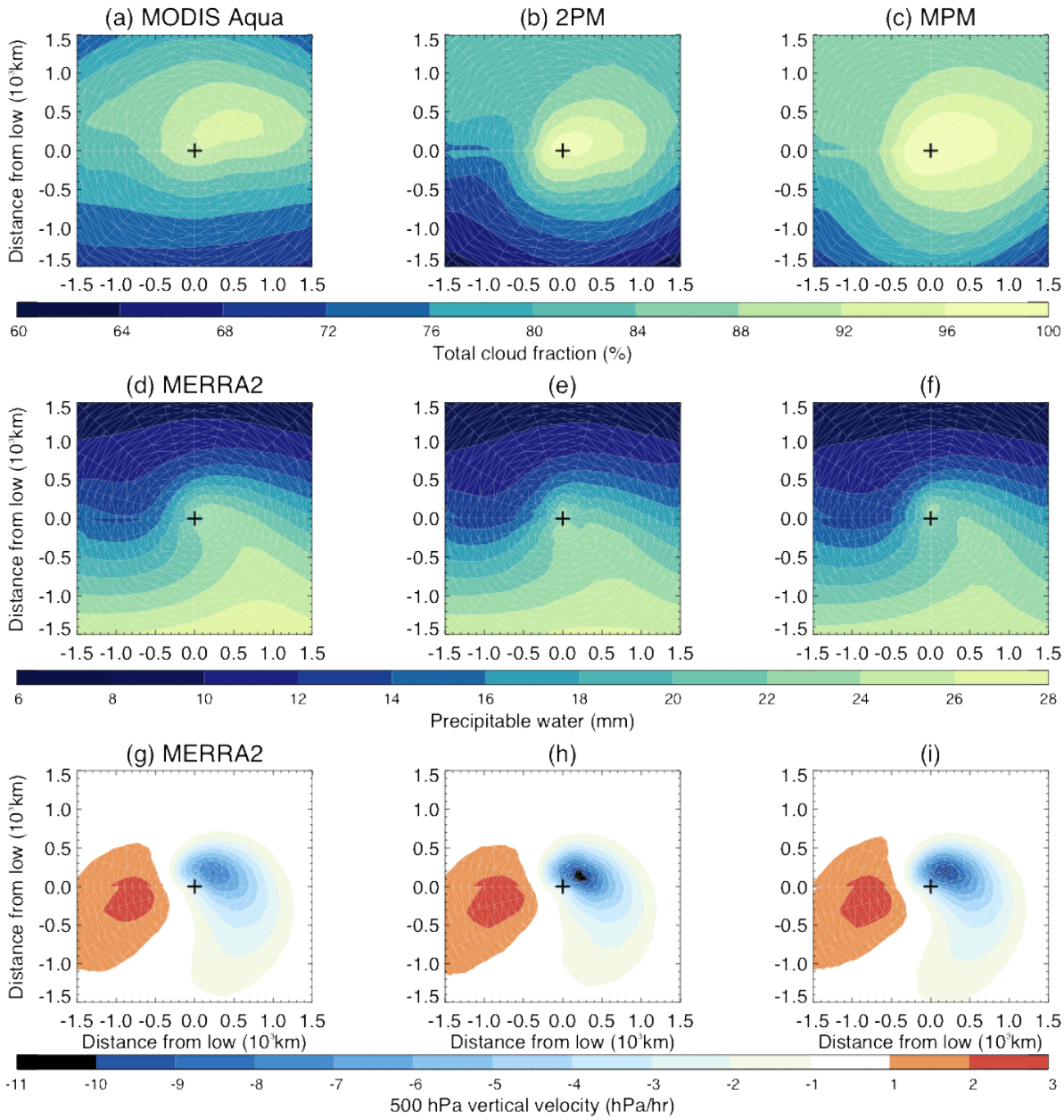

796
797 *Figure 3: Cyclone-centered composites of (a,b,c) total cloud cover, (d,e,f) PW and (g,h,i) 500 hPa*
798 *vertical velocities from (a) MODIS, (d, g) MERRA-2, (b, e, h) 2PM and (c, f, i) MPM, for SH*
799 *cyclones in November-March.*

800

Accepted for publication in *Journal of Climate*. DOI 10.1175/JCLI-D-19-0421.1.

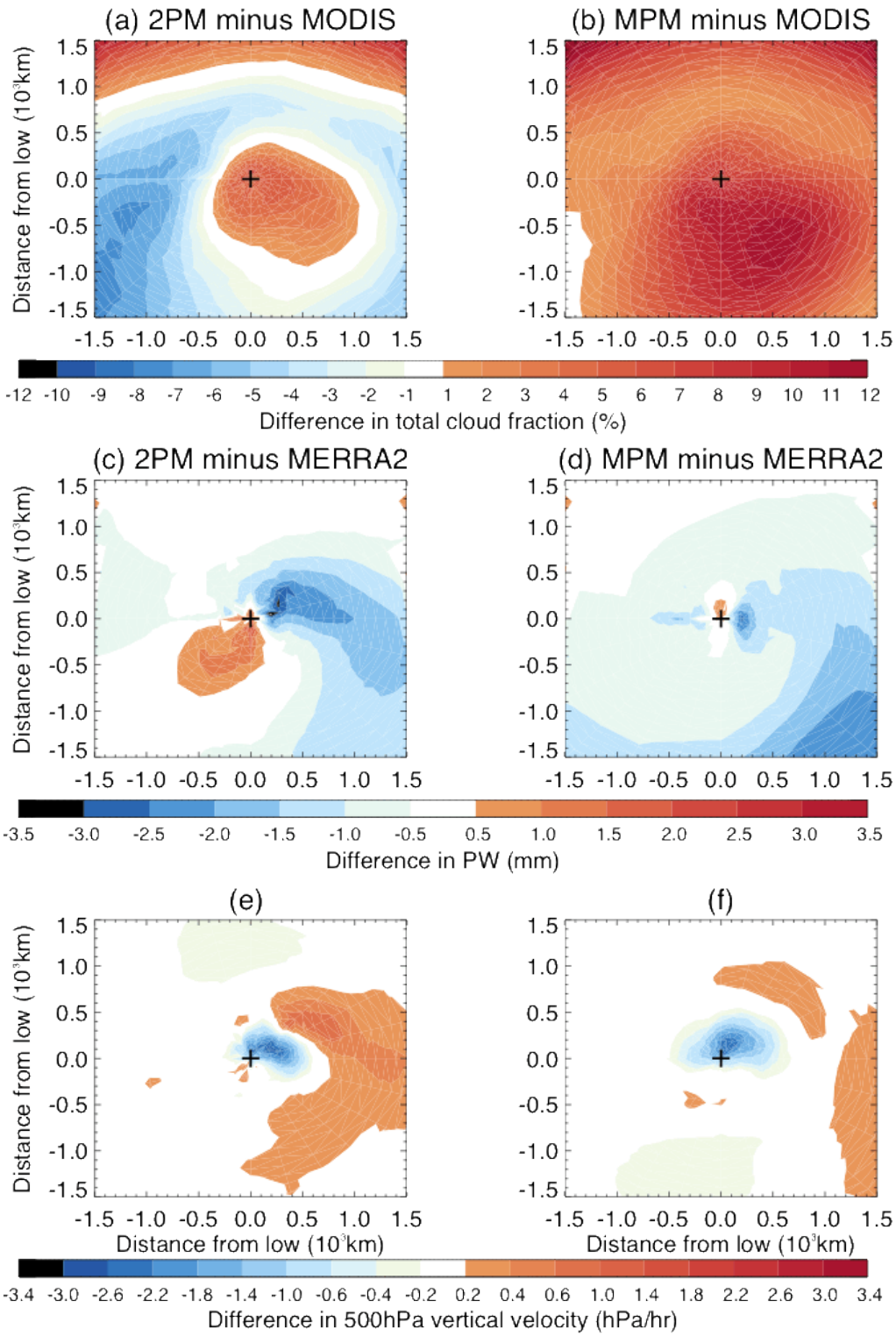

Figure 4: Difference in cyclone-centered composites of cloud cover (a-b), PW (c-d) and 500 hPa vertical velocities (e-f) between (a, c, e) 2PM and (b, d, f) MPM and MODIS/MERRA2, for SH cyclones in November-March.

Accepted for publication in *Journal of Climate*. DOI 10.1175/JCLI-D-19-0421.1.

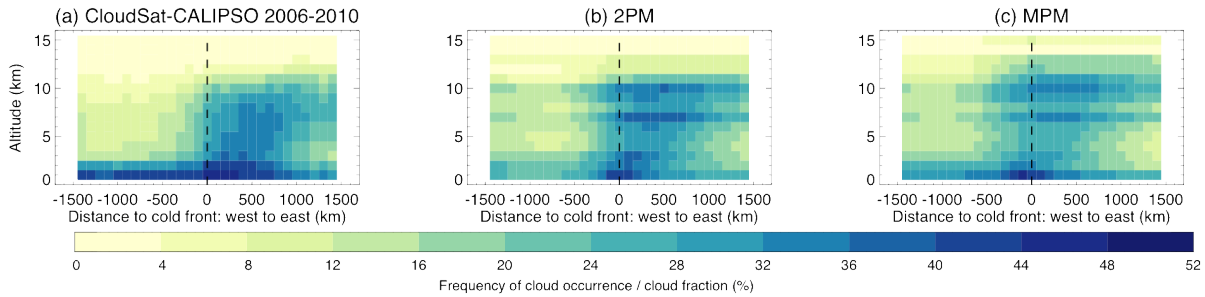

Figure 5: Cold front centered composites of vertical cloud distribution from (a) CloudSat-CALIPSO averaged over 2006-2016, (b) as modeled with devAM4 2PM and (c) as modeled with devAM4-MPM. The vertical dashed line indicates the location of the surface front: the post-cold frontal or cold side of the front is to the left of this line, while the pre-cold frontal or warm side of the front is to the right. These are southern hemisphere cold fronts during November-March.

Accepted for publication in *Journal of Climate*. DOI 10.1175/JCLI-D-19-0421.1.

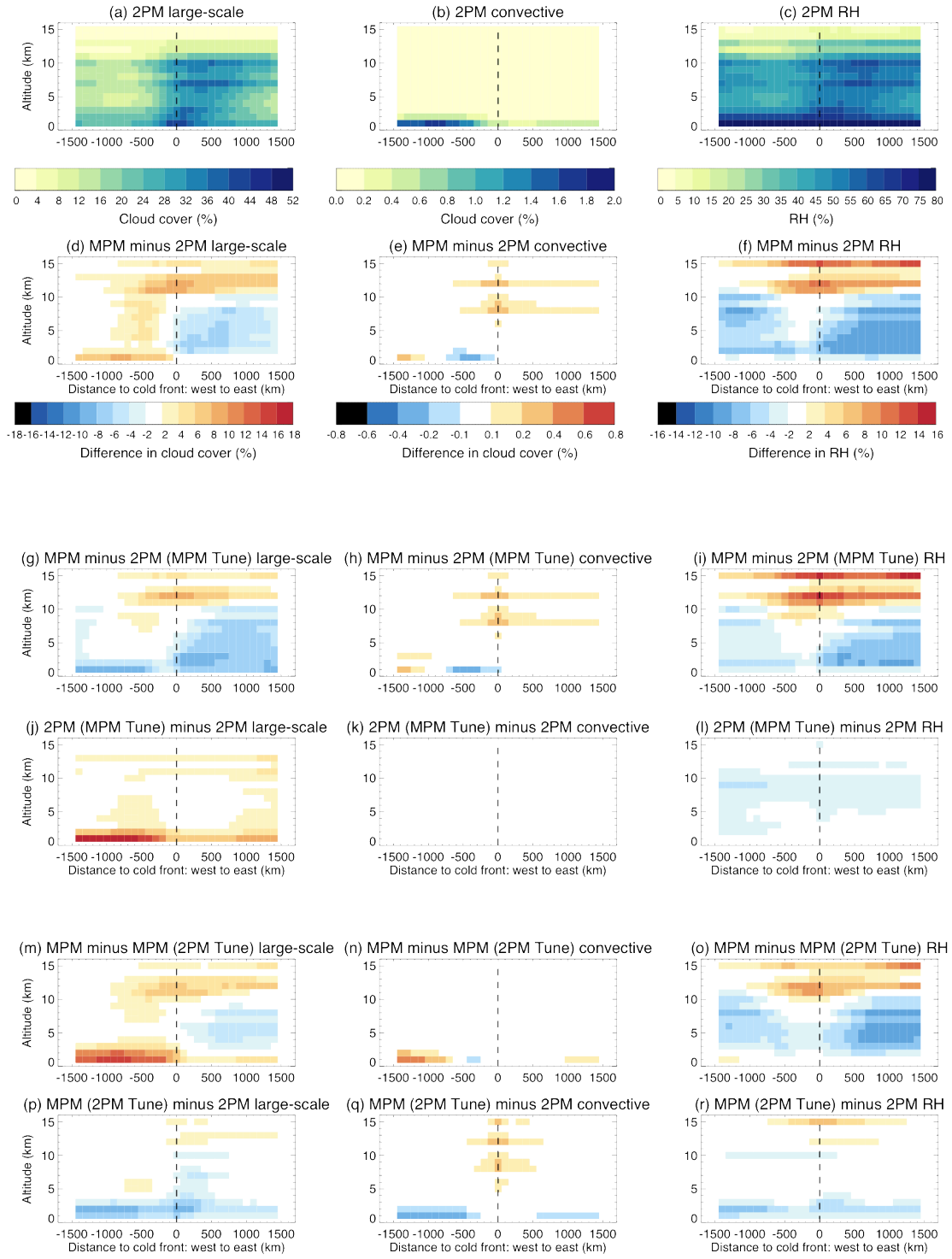

Figure 6: Cold-front centered composites of the 2PM (a) large-scale and (b) convective cloud cover, and (c) RH, and difference in large-scale cloud cover, convective cloud cover and RH between: MPM and 2PM (d, e, f); MPM and 2PM (MPM Tune) (g, h, i); 2PM (MPM Tune) and 2PM (j, k, l); MPM and MPM (2PM Tune) (m, n, o); MPM (2PM Tune) and 2PM in (p, q, r). The vertical dashed line indicates the location of the surface front: the post-cold frontal or cold side

Accepted for publication in *Journal of Climate*. DOI 10.1175/JCLI-D-19-0421.1.

819 *of the front is to the left of this line, while the pre-cold frontal or warm side of the front is to the*
820 *right. These are southern hemisphere cold fronts during November-March.*

821
822

Accepted for publication in *Journal of Climate*. DOI 10.1175/JCLI-D-19-0421.1.

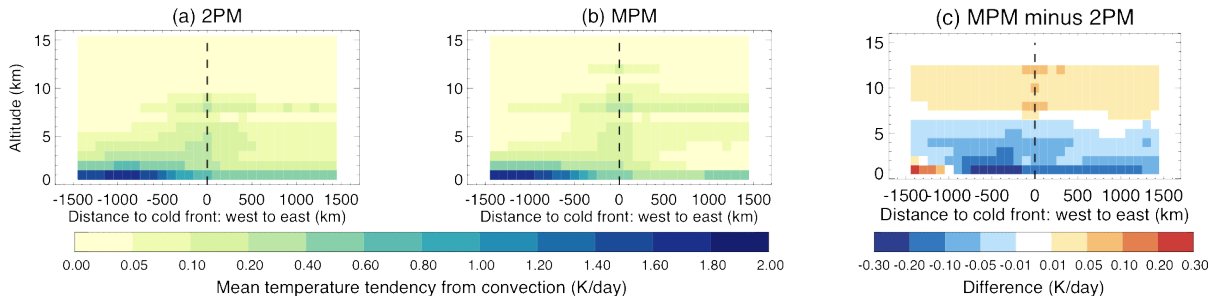

Figure 7: Cold front centered composites of temperature tendencies for convection from (a) 2PM, (b) MPM and (c) the difference between MPM and 2PM. The vertical dashed line indicates the location of the surface front: the post-cold frontal or cold side of the front is to the left of this line, while the pre-cold frontal or warm side of the front is to the right. These are southern hemisphere cold fronts during November-March.

Accepted for publication in *Journal of Climate*. DOI 10.1175/JCLI-D-19-0421.1.

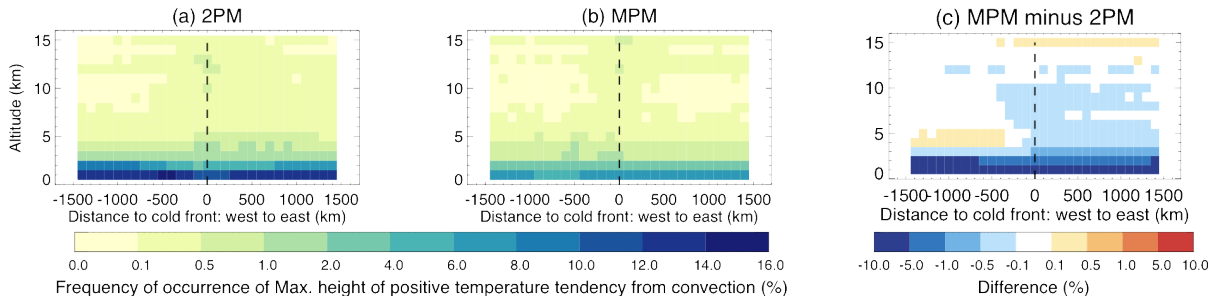

Figure 8: Cold front transect vertical distribution of the maximum height of the convective column in (a) 2PM, (b) MPM and (c) difference in height between MPM and 2PM. The vertical dashed line indicates the location of the surface front: the post-cold frontal or cold side of the front is to the left of this line, while the pre-cold frontal or warm side of the front is to the right. These are southern hemisphere cold fronts during November-March.

Accepted for publication in *Journal of Climate*. DOI 10.1175/JCLI-D-19-0421.1.

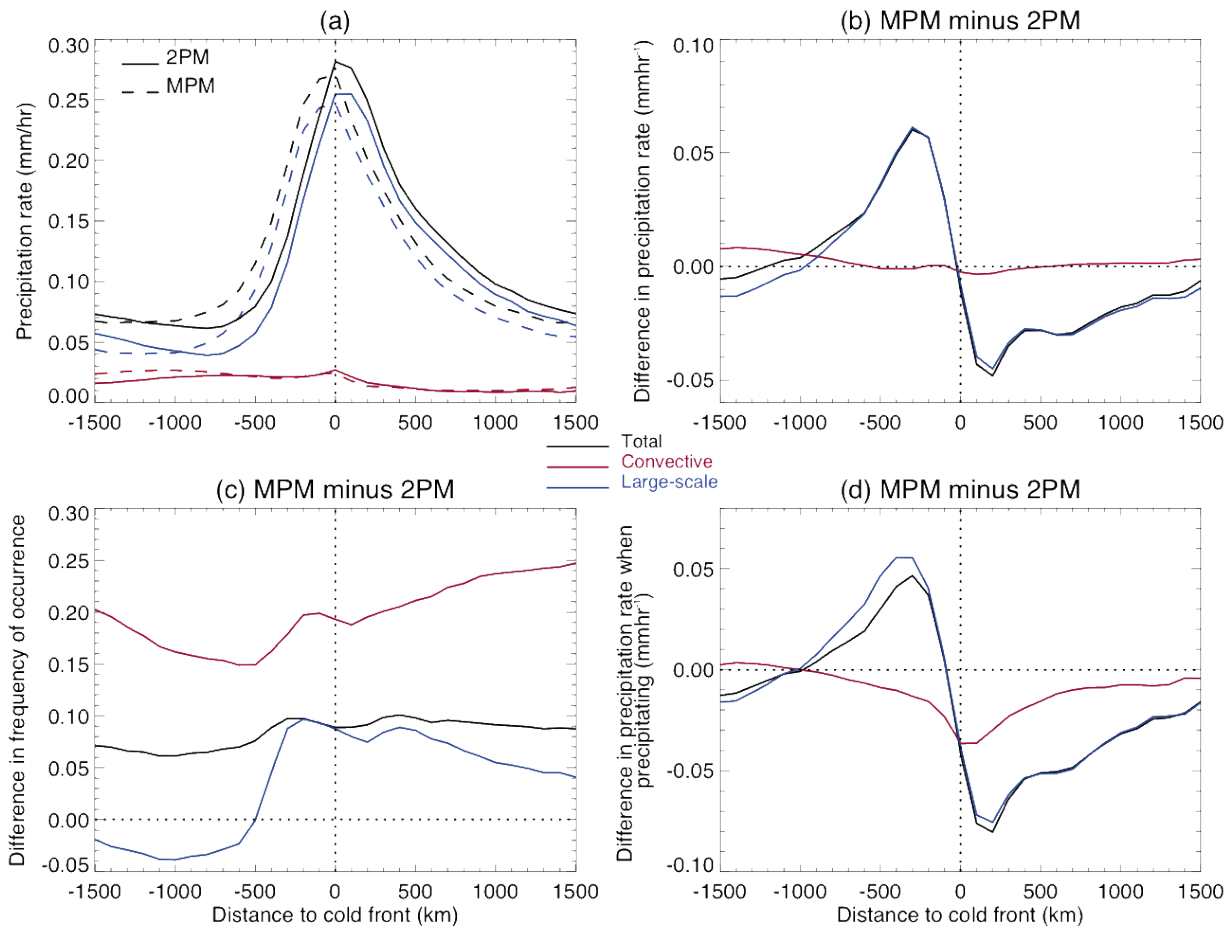

Figure 9: Cold front centered composite of (a) mean precipitation for 2PM (solid) and MPM (dashed) for total (black), convective (red) and large-scale (blue) precipitation and difference between MPM and 2PM in (b) mean precipitation, (c) frequency of precipitation and (d) precipitation rate when precipitating . The vertical dashed line indicates the location of the surface front: the post-cold frontal or cold side of the front is to the left of this line, while the pre-cold frontal or warm side of the front is to the right. These are southern hemisphere cold fronts during November-March.

Accepted for publication in *Journal of Climate*. DOI 10.1175/JCLI-D-19-0421.1.